Thermal Modeling of Patient-Specific Breast Cancer With Physics-Based Artificial Intelligence

I. Perez-Raya[1]
Mechanical Engineering Department,
Rochester Institute of Technology,
Rochester, NY 14623;
BiRed Imaging, Inc.,
Rochester, NY 14604
e-mails: ibpeme@rit.edu;
iperez@biredimaging.com

S. G. Kandlikar[1]
Mechanical Engineering Department,
Rochester Institute of Technology,
Rochester, NY 14623;
BiRed Imaging, Inc.,
Rochester, NY 14604
e-mails: sgkeme@rit.edu;
skandlikar@biredimaging.com

Breast cancer is a prevalent form of cancer among women. It is associated with increased heat generation due to higher metabolism in the tumor and increased blood vessels resulting from angiogenesis. The thermal alterations result in a change in the breast surface temperature profile. Infrared imaging is an FDA-approved adjunctive to mammography, which employs the surface temperature alterations in detecting cancer. To apply infrared imaging in clinical settings, it is necessary to develop effective techniques to model the relation between the tumor characteristics and the breast surface temperatures. The present work describes the thermal modeling of breast cancer with physics-informed neural networks. Losses are assigned to random points in the domain based on the boundary conditions and governing equations that should be satisfied. The Adam optimizer in TensorFlow minimizes the losses to find the temperature field or thermal conductivity that satisfies the boundary conditions and the bioheat equation. Backpropagation computes the derivatives in the bioheat equation. Analyses of the three patient-specific cases show that the machine-learning model accurately reproduces the thermal behavior given by ANSYS-FLUENT *simulation. Also, good agreement between the model prediction and the infrared images is observed. Moreover, the neural network accurately recovers the thermal conductivity within 6.5% relative error.* [DOI: 10.1115/1.4055347]

Keywords: breast cancer, infrared imaging, PINN modeling, breast cancer detection, AI model

1 Introduction

Breast cancer remains a significant cause of morbidity and mortality in women. 30% of cancer diagnosed in women in 2021 was breast cancer, and about 1 in 8 U.S. women will develop invasive breast cancer in their lifetime [1]. Early detection is critical in effectively treating and avoiding the spread of cancer to other body regions. Infrared imaging is an FDA-approved adjunctive to mammography, which can benefit from machine learning (ML) for more effective screening. While much research focuses on developing diagnostic tools to screen breast cancer, a cost-effective and reliable technique based on infrared imaging is still elusive [2]. Thermal imaging can become an effective technology to screen patients for breast cancer safely, quickly, and inexpensively [3,4]. However, current thermal imaging depends on computer modeling of a breast to identify the relation between the infrared images and the tumor characteristics. Available methods include theoretical solutions of the bioheat equation, computational fluid dynamics, boundary elements methods, and supervised artificial intelligence. The present work describes a novel approach based on physics-informed artificial intelligence to model breast cancer in patient-specific digital models.

Researchers apply theoretical solutions of the bioheat equation to model breast cancer and relate the tumor location and heat generation to the surface temperatures. Assumptions include the representation of the tumor with a point source, tumor located along a defined axis, and homogenous breast tissue. Gescheit et al. [5] simulated heated nanoparticles inside a rectangular domain and accurately related the surface temperature to the heat source magnitude and predicted the depth within 4.2%. Han et al. [6] theoretically modeled breast cancer to relate temperatures from an infrared camera of four patients with dense breasts to the magnitude of the metabolic heat generation. Results revealed that the strengths of the heat sources in malignant cases were significant and enabled clear identification of the tumor. Ye and Shi [7] theoretically modeled breast cancer to develop a method that identified soft (low heat generation) and malignant (high heat generation) tumors. Rastgar and Mohammadi [8] theoretically modeled breast cancer and applied artificial neural networks (ANNs) to find the tumor heat generation; the predicted maximum temperature was in good agreement with thermographic data. Akpolile et al. [9] theoretically solved the bioheat equation to identify the thermal behavior of deep-seated tissues in the body. One of the main drawbacks of applying theoretical solutions lies in the inability to model patient-specific breast cases, which reduces the accuracy in detecting the tumor characteristics.

Numerical simulations based on computational fluid dynamics (CFD) provide another alternative to model breast cancer. The method performs accurate modeling of patient-specific breast digital models. However, the need of multiple commercial software to create the computational grid and numerically solve the bioheat equation prevents its application in clinical settings. Mitra and Balaji [10] trained ANNs with 375 simulated training cases and 72 simulated validation cases of a hemispherical breast with a spherical tumor located along the central axis. The ANNs used 49 inputs (surface temperatures) and 4 outputs (tumor location and radius). Results showed minor prediction errors of 15 and 22% in tumor location. Saniei et al. [11] performed 70 simulated training cases and 25 simulated validation cases of 4 different spherical tumors. The trained NN predicted a tumor size of 1.59 cm and a tumor depth of 1.1 cm against actual values of 2.5 cm and 1.5 cm for one of the patients. Hossain and Mohammadi [12] used genetic algorithms (GA) to simultaneously determine an embedded tumor's depth, radius, and heat generation. Predictions with 10% noise in the numerical breast surface temperatures showed

[1]Corresponding authors.

Contributed by the Heat Transfer Division of ASME for publication in the JOURNAL OF HEAT AND MASS TRANSFER. Manuscript received June 20, 2022; final manuscript received August 13, 2022; published online December 9, 2022. Assoc. Editor: Yogesh Jaluria.

average errors of 3%. The data was generated from computer modeling of a hemispherical or a hemispherical-deformed breast. Parush and Majchrzak [13] performed numerical simulations to develop an inverse model that identifies tissue properties or tumor size and location. Results indicated maximum errors with a hemispherical breast shape of 0.4%. Das and Mishra [14] performed simulations to develop an inverse model. The authors found an exact prediction of blood perfusion rate while keeping all other parameters known. Also, relative errors of 2.5% in the predicted tumor location and 5.5% in the predicted tumor size were achieved. Hatwar and Herman [15] performed breast modeling with seven layers of different thermal properties and developed an inverse method. The steady-state prediction used 12 data points distributed in a region above the tumor. Steady-state analyses with the three unknowns (radius, depth, and blood perfusion) showed different combinations of the tumor parameters yielding nearly identical thermal signatures. The transient study with three unknowns showed maximum errors of 0.017% within 34 iterations. Figueiredo et al. [16] developed a linear regression model. For each tumor identification, 1401 tumors of specific diameters located within a search region were simulated individually. Results indicated maximum errors for geometric center estimation of 0.32 cm for a cancer of 1 cm in diameter located at 5 cm from the surface; the time required to perform the prediction was between 39 to 86 min. In Bezerra et al. [17], simulations revealed effects of the breast density, specific heat, tumor blood perfusion, and tumor thermal conductivity on the breast surface temperature. The inverse method showed relative errors of 1.8 and 4.2% on the tissue conductivity and blood perfusion rate prediction. Agnelli et al. [18] developed a pattern search algorithm; results with 15% noise in a hemispherical breast showed relative errors of 5.8% and 5.5% in predicting the tumor metabolic heat rate and location. Gonzalez-Hernandez et al. [19] coupled infrared imaging, computer simulations, and the inverse Levenberg-Marquardt algorithm to accurately identify the location and size of cancerous breast tumors in seven patients. Other works focus on generating computer simulations of patient-specific digital breast models [20–22]. Also, researchers have adopted computer simulations to analyze the effect of blood flow and thermal behavior in anatomical vessels [23–25].

Other techniques to couple cancerous tumor modeling with infrared imaging consider boundary element methods. An in-house code is required to solve the equations and the method has not been tested in patient-specific breast shapes. Partridge and Wrobel [26] coupled GA with the dual reciprocity boundary element method (DRBEM). The model predicted a location of (0.0191 m, 0.0002 m) and a size of 0.0125 m × 0.025 m against actual values of (0.01 m, 0 m) and 0.01 m × 0.02 m. Luna et al. [27] developed a DRBEM coupled with simulated annealing. The method simultaneously predicted tumor location, size, blood perfusion rate, and metabolic heat generation in five tumors. Results showed that the noisy cases had a maximum relative error of 1% to 3%. Agnelli et al. [28] proposed a functional geometry algorithm that depended on the derivative of the objective function. The tumor was spherical in a rectangular domain. Results showed predictions of the tumor region with less than 2% relative errors.

Artificial intelligence models performing breast cancer detection utilize multiple infrared images to identify the presence of a tumor [29]. Mambou et al. [30] considered inputs of thermal images of 67 patients (43 healthy and 24 unhealthy) taken after cooling, and the output indicated the probability of cancer. Results show neural networks (NNs) classifying a thermal breast image as soft or malignant. Ng and Kee [31] demonstrated a similar approach in steady-state. Results showed 75% accuracy in making a proper diagnosis in the unhealthy population and 90% in the healthy population. Although these NN models can classify breast cancer cases, they cannot estimate the tumor location, radius, or breast tissue properties. Also, supervised AI models rely mainly on images and classification algorithms and ignore the governing bioheat equation to perform the training.

Recent advances include the development of a specific type of neural network called physics-informed neural network (PINN), utilizing physical constraints, boundary conditions, and governing equations of a naturally occurring phenomenon to define the loss functions [32–34]. The PINN learns the solution of differential equations by minimizing loss functions. The inputs to the neural network are the coordinates values of points in a domain, and the outputs are quantitative predicted values at these locations. The inputs and outputs include the coordinates of the points in the domain and information about these points, such as pressure, concentration, electric charge, and temperatures. PINNs are currently employed to uncover fluid dynamics or heat transfer trends [35,36], but to our knowledge, the technical literature lacks the application of PINNs to model systems with concentrated source terms, such as breast cancer with metabolic heat generation. PINNs main advantages over other available modeling techniques include

(1) Independence of commercial software for surface reconstruction, generation of computational grid, and physics modeling.
(2) High-level accuracy with a calculation of gradients using automatic differentiation (TensorFlow integrated function) rather than discretization techniques.
(3) Ability to retrieve optimal thermophysical properties (inverse modeling) such as thermal conductivity [37]. Inverse modeling for estimation of thermophysical properties can be done with regular NNs in combination with optimization techniques [38], and PINNs give a seamless approach to finding optimal parameters by simultaneously learning the physical conditions and surface temperatures.

The present work describes the application of PINNs to model breast cancer in patient-specific digital models. The main advantage lies in its ability to model breast cancer detection without commercial software to create a computational grid or solve governing equations. The developed PINN uses random points to find the solution and solves the bioheat equation with an optimizer. The model was created in TensorFlow (Google's AI platform). The present study applies PINN to thermally model three patient-specific cases. A sensitivity approach finds the optimal number of hidden layers and neurons. Results show that the PINN prediction closely approximates the temperatures of the computer simulation software. Also, the developed PINN generates temperature trends observed in infrared images obtained in a clinical setting. In addition, the PINN model finds tissue properties by defining a loss function of the surface temperatures.

2 Methods

This section describes the methods utilized to develop and test the proposed PINN. The PINN predictions were compared to results of a commercial CFD simulation software. Section 2.1 describes the techniques to reconstruct the patient-specific digital models and the tumor characteristics in the three analyzed cases, which had biopsy-proven breast cancer. Section 2.2 describes the methods to perform thermal modeling with PINNs including the definition of the loss functions fed to the optimizer. Section 2.3 focuses on the simulations used to evaluate the accuracy of the PINN model. Finally, Section 2.4 shows the equations used to evaluate the difference between the temperatures given by the simulation software and the developed PINN.

2.1 Reconstruction of Breast Digital Models and Tumor Characteristics. The digital breast model is a 3D surface file of the breast outline and shape. It is needed to perform both the CFD simulations and PINN modeling. In the present work, the digital breast models were reconstructed from available MRI images of the breast as described by Gonzalez-Hernandez et al. [19,21]. Figure 1 shows the computer-generated digital breast models adopted. Table 1 indicates the tumor characteristics including the

spatial location and radius. Available clinical data and MRI images gave the dimensions of the tumor characteristics (location and size) based on data from mammogram scans [39].

2.2 Physics-Based AI Algorithm. Figure 2 shows the points in the breast of Patient-2 used to perform the PINN modeling. The points are randomly generated from the digital breast model. The number of points depends mainly on the size of the surface area, the volume of the region, the length of the temporal domain, and the conditions or equations related to the modeling of the property in the system. The present work analyzes the effect of the number of points by looking at how the predicted specific property changes with the number of points.

Figure 3 shows the process flow. Spatial points are generated wherein each point corresponds to a specific location on the breast boundary or internal tissue. The PINN uses a fully connected neural network where the inputs are the locations of the points, and the outputs are the predicted temperatures at the points corresponding to the tumor characteristics (size and location). The Adam optimizer in the TensorFlow machine-learning platform minimizes the values of losses at the points.

Following the work of Raissi et al. [34], the loss equals the difference between the expected and predicted values. Ideally, the loss should be equal to zero. In the case of boundary conditions, consider, for example, $T = T_{ch}$ at the chest point cloud; the loss is $res = T - T_{ch}$, where T is the variable that is being predicted. In the case of functions or equations at the interior points, for the exemplary case of $T = mx + b$, the residual is $res = T - mx - b$, where T is the variable that is being predicted and x is the input to the NN. In the developed PINN, the optimizer minimizes the total loss given by

$$\text{loss}_T = \frac{1}{N_{BC}} \sum_{j=1}^{N_{BC}} (\text{loss}_{BC,j})^2 + \frac{1}{N_{inter}} \sum_{i=1}^{N_{inter}} (\text{loss}_{inter,i})^2 \quad (1)$$

where N_{BC} and N_{inter} correspond to the number of boundary and interior points.

The term loss_{BC} accounting for the boundary conditions is calculated from the conditions of convection at the breast surface and constant body temperature at the body chest ($T = T_{ch}$) [40]

$$\text{loss}_{BC1} = \frac{k}{D} \frac{\partial T^*}{\partial n^*}\bigg|_{pred} - h\left(T^*_{\infty} - T^*_{pred}\right) \quad (2)$$

Table 1 Tumor location and size in the analyzed patients

Tumor parameters	Patient-1	Patient-2	Patient-3
x-location (m)	0.076	0.058	0.053
y-location (m)	0.060	0.068	0.048
z-location (m)	0.118	0.13	0.125
Diameter (m)	0.014	0.008	0.011

$$\text{loss}_{BC2} = T^*_{ch,pred} - T^*_{ch} \quad (3)$$

The term $\text{loss}_{inter,i}$ is calculated from the dimensionless Pennes Bioheat equation, Eq. (4)

$$\text{loss}_{inter} = \frac{\partial^2 T^*}{\partial x^{*2}} + \frac{\partial^2 T^*}{\partial y^{*2}} + \frac{\partial^2 T^*}{\partial z^{*2}} + \frac{\rho c}{k}\omega_b D^2 (T_a{}^* - T^*) + \frac{2D^2}{k(T_{max} - T_{min})}\dot{q}_m \quad (4)$$

In Eqs. (1)–(4), T_a, $\dot{q}_m$, ω, ρ, c_p, k, and h, stand for artery blood temperature, metabolic heat generation, blood perfusion rate, tissue density, tissue-specific heat, tissue thermal conductivity, ambient convective heat transfer coefficient, respectively. Conventional thermal property values were adopted for each of the terms in the governing equations and boundary conditions [40].

The inverse problem considers the bioheat equation with unknown thermal conductivity. The PINN finds the thermal conductivity by minimizing the total loss, which includes the bioheat equation with an unknown thermal conductivity. Pashaei-Kalajahi et al. [37] enabled PINNs to predict the values of multiple intrinsic parameters (or properties) from data of the flow transport and the physics governing equations as part of its training.

Traditional deep learning models use several breast images to classify an IR image as healthy or cancerous [41–49]. These methods do not consider individual variability in patients as they overlook the basic governing equations for training and require excessive processing time due to a large amount of data [43,46,49]. Additionally, classification methods cannot identify the spatial location and size of the tumor.

In TensorFlow, the function tf.gradients calculated the derivatives with back propagation. The advantage lies in the ability to compute gradients using automatic differentiation, which eliminates numerical approximations limited by computational cell

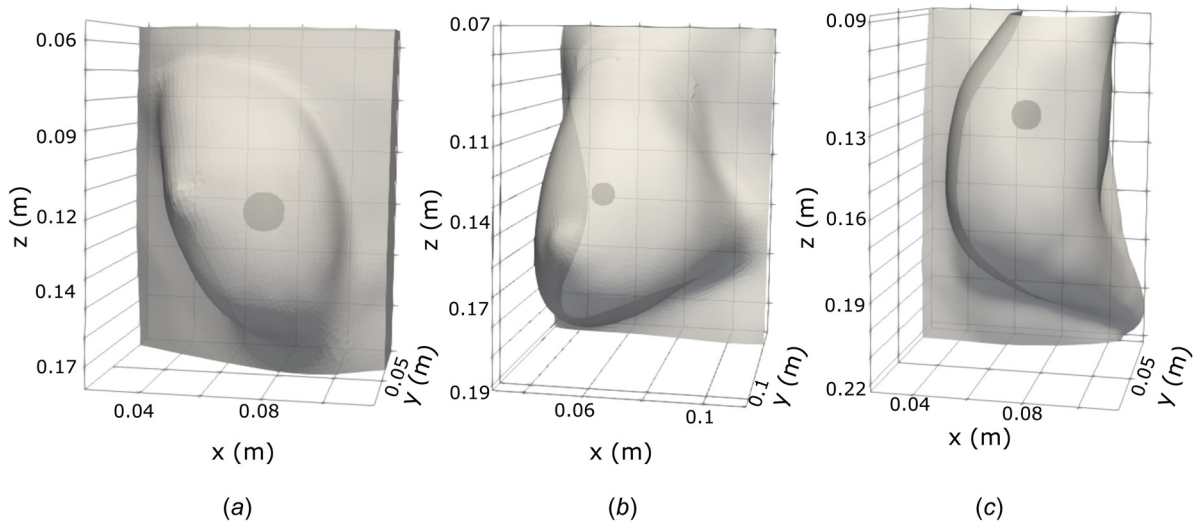

Fig. 1 Analyzed breast digital models with the identified tumor location and size: (*a*) patient-1, (*b*) patient-2, and (*c*) patient-3

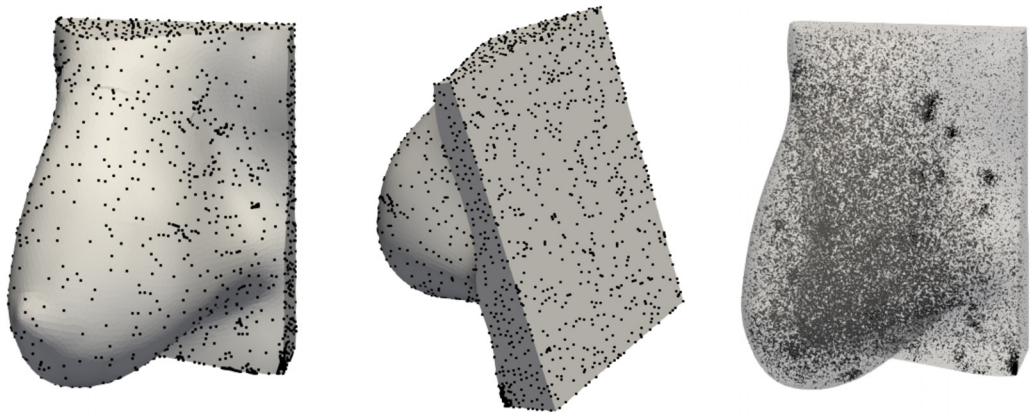

(*a*) (*b*) (*c*)

Fig. 2 Point clouds used for thermal modeling of the case Patient-2: (*a*) front view of surface points, (*b*) back view of chest points, and (*c*) front view of interior points

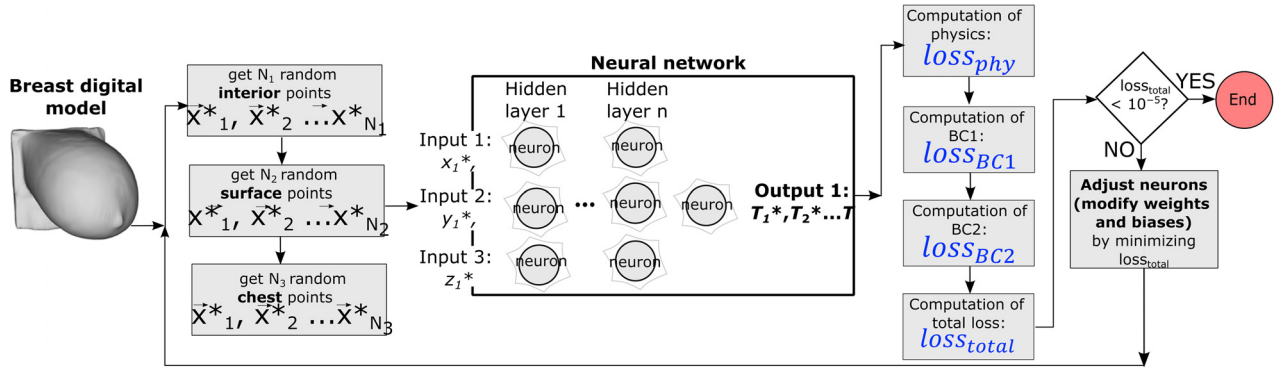

Fig. 3 Process flow and algorithm to perform breast cancer thermal modeling

size. An Nvidia Quadro RTX 8000, 48GB GPU executed the neural network model training.

2.3 Computer Simulation With Computational Fluid Dynamics. The commercial software ANSYS 2021R1 performed the simulation. Modules SpaceClaim and ANSYS-meshing created the computational grid representing the idealized 3D geometry. A grid with 1 million computational cells was made for each patient-specific digital model. The simulation of the thermal behavior due to the tumor was performed in ANSYS-FLUENT with central differences discretization scheme to estimate the gradients (in the governing equation) and TVID to solve the numerical matrices. Gonzales-Hernandez et al. [19] give additional details of the computer simulation in ANSYS-FLUENT.

The CFD model was validated by comparison of simulated surface and IR temperatures of seven patients with biopsy-proven breast cancer. Gonzalez-Hernandez [21] showed that the Pennes bioheat model generated the experimental internal tissue temperatures reported by Gautherie [50]. Recinella et al. [39] validated screening, digital model generation, and numerical modeling by comparison against infrared images of three women with biopsy-proven breast cancer. Gonzalez-Hernandez et al. [19] performed inverse modeling and identified acceptable agreement between CFD temperatures and IR images in seven patients. Also, a similar modeling approach shows good agreement of simulated and IR temperatures on realistic female torsos [22,51].

Table 2 shows the thermophysical properties in the CFD and PINN modeling. The adopted heat transfer coefficient (5 W/m^2-K) is justified since the patients were screened with the IR imaging system in an enclosed environment under ambient conditions, and a similar value was adopted in previous clinical studies [51]. Gautherie's experimental work [50] on determining breast tissue thermal conductivity shows a small range of thermal conductivity (0.17–0.37 W/m-K) depending on tissue structure. In addition, the modeling assumed a homogenous thermal conductivity since the difference in thermal conductivity between cancerous and normal tissue is minimal and the tumor region is small [50]. The hyperbolic relation between metabolic activity and tumor radius derived by Gautherie [50] calculated the tumor heat generation based on the tumor radius.

2.4 Quantification of Difference Between Physics-Informed Neural Network and Computational Fluid Dynamics Results. The quantified difference between the temperatures obtained with PINN and CFD considered the absolute difference (AD) and the mean squared error (MSE). The AD calculated by Eq. (5) shows a distribution of the difference between the predicted and the expected temperatures.

$$\mathrm{AD}_i = |T_{\mathrm{pred},i} - T_{\mathrm{CFD},i}| \tag{5}$$

where $T_{\mathrm{pred},i}$ corresponds to the temperature predicted by the PINN model at point i and $T_{\mathrm{CFD},i}$ is the temperature given by the CFD model at point i.

The MSE given by Eq. (6) gives an average value of the difference between the CFD and PINN temperatures. The MSE is always positive, and values close to zero imply more relative similarities

$$\mathrm{MSE} = \frac{1}{N}\sum_{i=1}^{N}(T_{\mathrm{pred},i} - T_{\mathrm{CFD},i})^2 \tag{6}$$

where N corresponds to the number of points.

3 Results

Section 3.1 shows the computed errors obtained in the identification of the optimal number of layers and neurons. Section 3.2 demonstrates the accuracy of the developed PINN model relative to temperatures obtained with a customized computer model. Section 3.3 shows the ability of the PINN in generating temperature trends in infrared images obtained in clinical settings. Finally, Section 3.4 shows the way the PINN model performs inverse modeling to predict the tissue thermal conductivity.

3.1 Neuron, Layers, and Points Sensitivity Analysis (Identification of Optimal Physics-Informed Neural Network). Sensitivity analyses identified the optimal configuration. The analysis of number of hidden layers and neurons determined an optimal neural network configuration capable of giving an MSE lower than 0.1. The analysis of number of hidden layers and neurons considered a fixed number of points equal to 22,000 in the interior, 2,000 on the surface, and 2,000 on the chest.

Table 3 shows the results obtained for each test case after 500,000 training iterations. Results show the number of hidden layers and neurons playing a significant role in the accuracy of the predicted temperature. Results also show improved accuracy by increasing the number of hidden layers from 1 to 3 and the number of neurons from 10 to 30. Results indicate that the configuration with 3 hidden layers and 30 neurons can reach the desired MSE lower than 0.1.

Figure 4 shows the results of quantifying the effect of the interior points and the number of iterations. Figure 4(*a*) shows the computed MSE for Patient-1 with 22,000, 12,000, and 7,000 interior points with 3 hidden-layers and 30 neurons. Figure 4(*b*) shows the MSE computed for each analyzed patient-specific digital model with the adopted PINN configuration. Results in Fig. 4(*a*) reveal that the PINN performs an accurate prediction after 250,000 iterations for the three analyzed number of interior points. However, the initial error is significantly higher with fewer interior points.

Although the configuration with the lowest number of interior points reached a low MSE at the end of the 500,000 iterations, we preferred to follow a safe path. Therefore, the PINN with 3 hidden layers and 30 neurons with 22,000 interior points was adopted to perform subsequent analyses since it gave the lowest MSE during training, including an early stage in the training process. Results in Fig. 4(*b*) show MSE values obtained during the training of the cases Patient-1, Patient-2, and Patient-3 with the adopted neural network configuration. The developed PINN gave an MSE that decreased from 0.1 early in the training process to 0.04 after 1 million iterations. These results indicate that the adopted PINN configuration performs well for the three analyzed patient-specific cases.

Table 2 Thermophysical properties and conditions adopted by the simulation and PINN modeling

Parameter	Value	Unit
Thermal conductivity (k) [51]	0.3	W/m-K
Perfusion rate of healthy tissue (ω_h) [51]	1.8×10^{-4}	1/s
Perfusion rate of tumor (ω_t) [51]	9×10^{-3}	1/s
Metabolic activity of healthy tissue ($\dot{q}_h$) [51]	450	W/m^3
Metabolic activity of tumor ($\dot{q}_t$) [51]	5,000-70,000	W/m^3
Temperature of arteries (T_a) [53]	37	°C
Specific heat of blood (c_b) [53]	3,840	J/kg-K
Density of blood (ρ_b) [53]	1,060	Kg/m^3
Core temperature (T_c) [51]	37	°C
Ambient temperature (T_∞)	21	°C
Heat transfer coefficient (h) [52]	5	W/m^2-K

3.2 Comparison Simulations With Computational Fluid Dynamics and Predictions With Physics-Informed Neural Network. Figure 5 shows a comparison of the breast surface temperatures retrieved by ANSYS-FLUENT and PINN. The boundary conditions of 310 K at the chest and 294 K at the ambient drive the breast surface temperature distribution. The temperature distribution on each patient shows maximum values of 309 K near the chest and a minimum value of 302 near the outer region. The tumor metabolic heat generation creates an area of increased temperature on the east side in Patient-1, west side in Patient-2, and northeast side in Patient-3. The tumor metabolic heat generation increases the temperature by approximately 1 K. These results show that the PINN model can reproduce the main features related to the breast cancer thermal behavior. In addition, results show that the developed PINN can generate the temperatures given by CFD. Similar levels of accuracy of PINNs against CFD have been reported by recent works modeling blood flow in brain aneurysms [53], fluid dynamics in laminar flow [55], and heat transfer [35].

Figure 6 shows the absolute difference in breast surface temperature between CFD and PINN for the case Patient-1. The figure reports the change in the AD (calculated with Eq. (5)) with the number of iterations. Results show the highest AD changing from 0.74 at 100,000 training iterations to 0.3 at 1 million iterations. At 100,000 iterations, results show significant absolute differences in the regions near the chest. However, this trend reverses after 200,000 iterations since Figs. 6(*b*)–6(*d*) show the lowest AD values near the breast chest. A possible explanation is that the PINN might perform early identification of the regions with high errors; it might be focusing most of the rest of the training on the early-identified areas of high error.

3.3 Comparison of Physics-Informed Neural Network Against Infrared Temperatures. We compared the predicted temperatures with infrared images to further evaluate the ability of the PINN to model breast cancer. The infrared pictures were obtained with the clinical imaging system described in previous works [19,39].

Figure 7 shows a comparison of the infrared image data with the PINN predictions. The temperature contours given by the developed PINN were obtained by adjusting the breast digital model to match the infrared images. Also, the temperature range in the images obtained from the PINN model was adjusted to match the infrared images. Overall, there is good agreement between the infrared and the predicted temperatures in terms of magnitude and temperature distribution. In Patient-1, both the PINN and infrared results show an increased temperature of 305.6 K in the breast surface region due to the tumor metabolic heat generation. In Patient-2, infrared image shows a spot with a high temperature near the nipple, and PINN shows a larger area with a high temperature near the nipple. In addition, the temperature decays from 306 to 302 K and follows the same trend in both infrared and PINN. Similar results are observed in Patient-3 where the PINN and infrared show an increased temperature with a value of 305 K on the breast surface at the northeast due to the tumor metabolic heat generation and a cold region of 302 K on the breast surface at the center. The differences between the PINN and IR temperatures arise from the modeling assumptions embedded in the Pennes bioheat equation and boundary conditions.

Table 3 Effect of the number of hidden layers and neurons in Patient-1

NN configuration	MSE error (500k iteration)	Total loss at MSE
1 Layer, 30 Neurons	1.809	3.84×10^{-3}
2 Layers, 30 Neurons	1.116	1.31×10^{-3}
3 Layers, 30 Neurons	0.028	1.51×10^{-4}
3 Layers, 20 Neurons	4.901	2.52×10^{-3}
3 Layers, 10 Neurons	5.216	2.75×10^{-3}

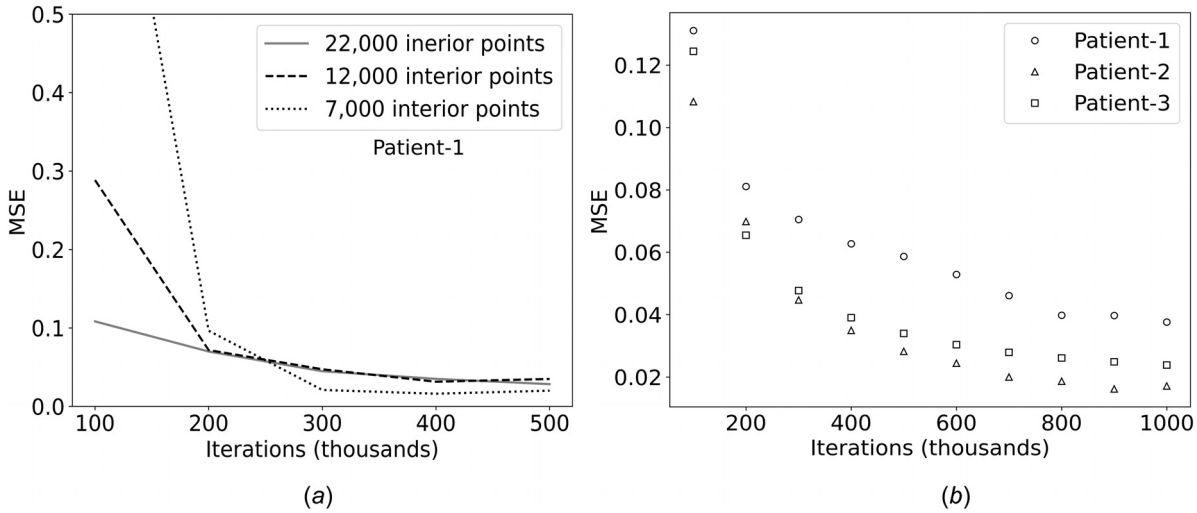

Fig. 4 Performance of PINN with three hidden layers and 30 neurons: (*a*) effect of the number of interior points in case Patient-1 and (*b*) impact of the number of iterations in cases Patient-1, Patient-2, and Patient-3

Assumptions such as homogeneous perfusion rate, tissue properties, and metabolic heat generation rate might be most influential [51]. Recent advances by Gershenson and Gershenson [55] show internal vasculature plays a vital role in the heat transfer from the tumor to the surface, which might influence the observed temperature differences. Nevertheless, the temperature predicted by the PINN model closely reproduces the infrared temperatures in the three analyzed cases. Results in Fig. 7 show (i) PINNs capturing the temperature range (maximum and minimum values) and distribution in the IR images, and (ii) PINNs identifying an increased temperature at surface regions due to the tumor presence given by the IR image. Still, IR images show more abrupt temperature variations, whereas PINN predicts more smooth temperature distributions. Further, IR images reflect the local variations due to surface vessels and other anomalies. It might be worth developing modeling techniques considering the biological aspects (perfusion rate and heat generation) and the effect of thermal properties and boundary conditions with more detail, which will allow

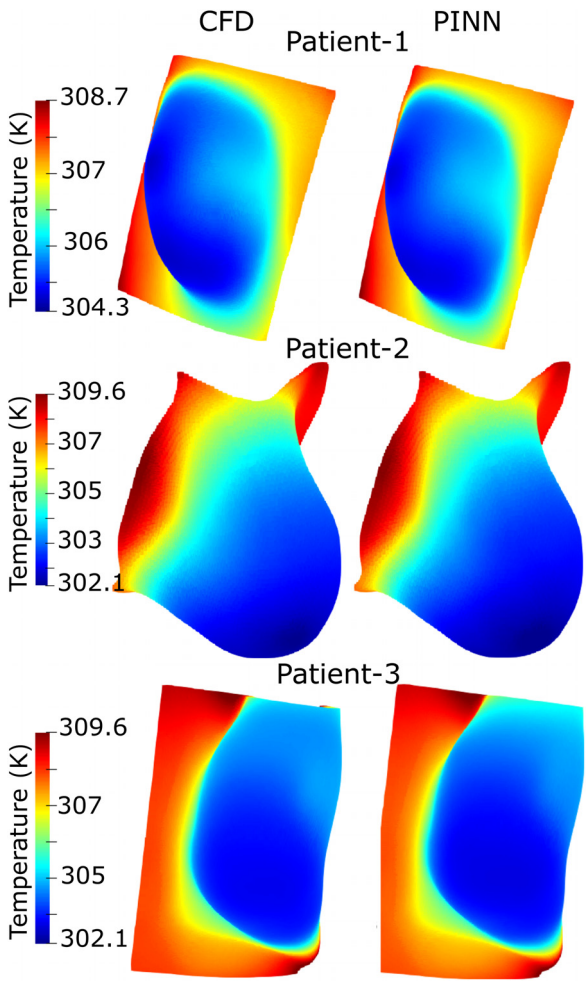

Fig. 5 Comparison of breast surface temperature obtained with the CFD software and the PINN model for the three analyzed patients

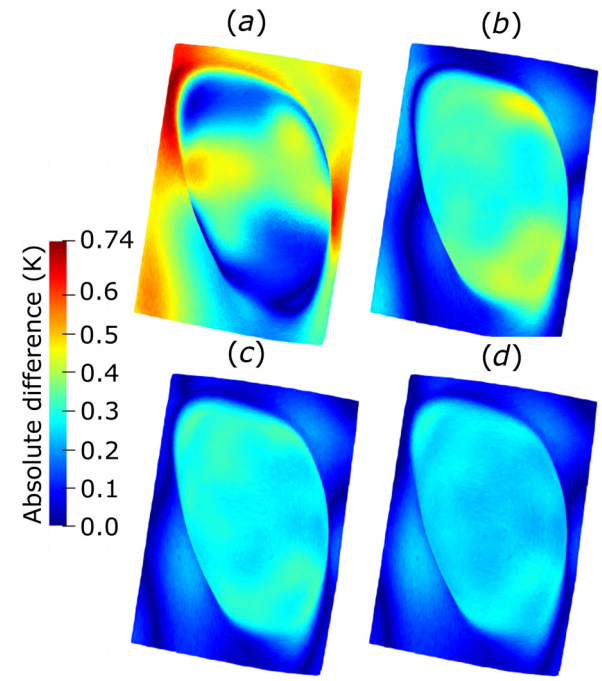

Fig. 6 Calculated absolute difference (AD) between PINN and CFD with the number of training iterations: (*a*) 100,000 iterations, (*b*) 400,000 iterations, (*c*) 700,000 iterations K, and (*d*) 1,000,000 iterations. Differences computed for Patient-1.

generating the sharp transitions in temperature on the surface observed in the IR images.

3.4 Retrieving Thermal Conductivity (Inverse Modeling). Another advantage of PINN over conventional CFD lies in the ability to perform inverse modeling. In forward modeling, the temperatures are obtained with specified thermal properties. In inverse modeling, the challenge involves getting the thermal properties given temperature values at specific points on the surface. The present investigation tested the ability of the PINN model to retrieve the tissue thermal conductivity assuming a known temperature of 1,000 points on the breast surface. The developed PINN finds the thermal conductivity value leading to a minimal total loss magnitude. The process requires an initial guess, predefined at 0.2 W/m-K with a target thermal conductivity of 0.3 W/m-K.

Results indicated that at the beginning of the training, the thermal conductivity is equal to 0.2, which is the predefined initial value. The PINN identifies that the optimal thermal conductivity is higher than the initial value during the first couple of iterations. Then, the PINN quickly increases to the value of 0.3 W/m-K after 20,000 iterations. Then, the change in the thermal conductivity becomes more asymptotic as the PINN gets closer to the target. After 120,000 training iterations, the thermal conductivity value has become fully asymptotic and constant with a predicted value of 0.32 W/m-K. It was assumed that the PINN model predicted a thermal conductivity of 0.32 W/m-K, which is 6.5% different from the target value of 0.3 W/m-K.

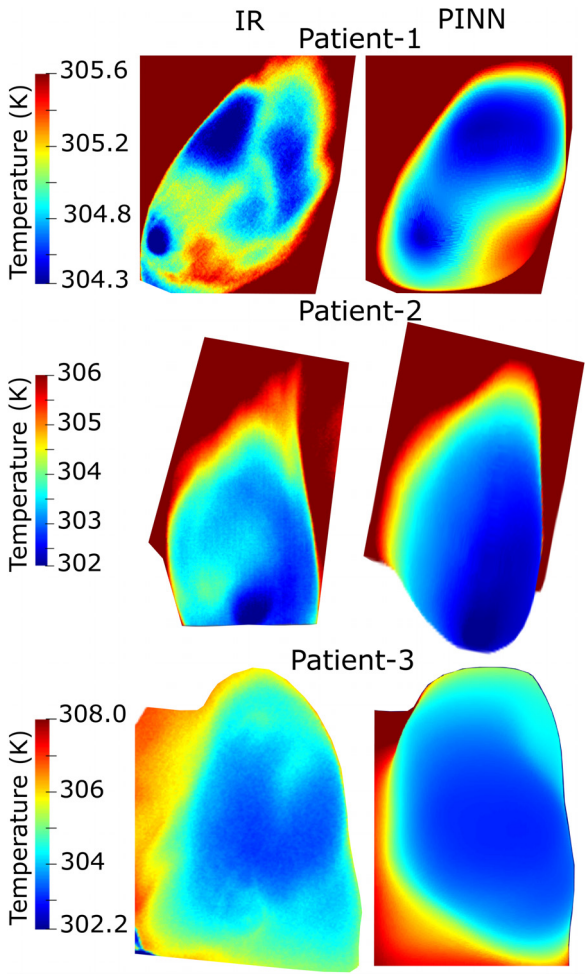

Fig. 7 Comparison between the prediction of the PINN model and infrared images for the three analyzed cases

4 Conclusions

The present work describes the application of a PINN in the thermal modeling of breast cancer. The developed PINN has successfully performed breast cancer thermal modeling including the inverse calculation of the tissue thermal conductivity. The developed approach uses a digital breast model to create random points. The points are employed to define losses related to the boundary conditions (a constant temperature at the chest and convection at the breast surface) and the governing equations (the bioheat equation at the interior). The PINN was implemented in TensorFlow and learned the thermal conditions (including the thermal tissue conductivity) by minimizing the losses with the Adam optimizer. The approach was tested with three patient-specific cases, and the predicted temperature distribution was compared against temperatures obtained from CFD.

The optimization method to identify the best neural network configuration indicated that only three hidden layers with thirty neurons are necessary to perform an accurate prediction. Also, results revealed that 7000 interior points could find an acceptable solution, but more points lead to low MSE values with fewer training iterations. The comparison of the developed physics-based AI model against the CFD solution showed MSE values below 0.1 within the first 150,000 iterations for each analyzed patient-specific case. Temperature contours showed that the developed model closely reproduced the thermal trends given by the CFD model. Also, a comparison with infrared images revealed that the PINN model generated temperature trends obtained in clinical settings. Finally, results indicated the capability of the PINN to retrieve the tissue thermal conductivity; the developed model predicted the tissue thermal conductivity with a 6.5% relative error within the first 120,000 training iterations.

The present study demonstrates that PINNs effectively predict breast cancer thermal behavior without the need for commercial software to create the computational mesh or perform the numerical simulation, which is a step toward implementing infrared technology in clinical settings. Moreover, the present work shows the validity of the PINN approach with actual patient data. Further large-scale clinical studies are warranted before the system can be established as an adjunctive screening modality to mammography that detects breast cancer in clinical settings.

Funding Data

- National Science Foundation (NSF) (Grant No.: # 2136325; Funder ID: 10.13039/100000001).

Nomenclature

AD = absolute difference in temperature (K)
c = specific heat (J/kg-K)
D = characteristic length (m)
H = convective heat transfer coefficient (W/m^2-K)
K = thermal conductivity (W/m-K)
loss = loss value fed to optimizer
MSE = mean squared error
N = number of points
n = unit normal vector
T = temperature (K)
$\mathbf{x}$ = vector with x, y, and z coordinates (m)
ρ = tissue density (kg/m^3)
ω = perfusion rate (1/s)

Superscripts or Subscripts

BC = boundary condition
ch = chest
int = interior
max = maximum
min = minimum

pred = predicted
* = dimensionless
∞ = ambient

References

[1] Weiss, M. C., Chick, E., Conner, K., DePolo, J., Lee, V., and Uscher, J., 2021, "U.S. Breast Cancer Statistics," Breastcancer.org [Online], accessed Oct. 13, 2021, https://www.breastcancer.org/symptoms/understand_bc/statistics

[2] Kandlikar, S. G., Perez-Raya, I., Raghupathi, P. A., Gonzalez-Hernandez, J.-L., Dabydeen, D., Medeiros, L., and Phatak, P., 2017, "Infrared Imaging Technology for Breast Cancer Detection – Current Status, Protocols and New Directions," Int. J. Heat Mass Transfer, **108**, pp. 2303–2320.

[3] Owens, A., Kandlikar, S. G., and Phatak, P., 2021, "Potential of Infrared Imaging for Breast Cancer Detection: A Critical Evaluation," ASME J. Med. Diagn., **4**(4), p. 041005.

[4] Gonzalez-Hernandez, J.-L., Recinella, A. N., Kandlikar, S. G., Dabydeen, D., Medeiros, L., and Phatak, P., 2019, "Technology, Application and Potential of Dynamic Breast Thermography for the Detection of Breast Cancer," Int. J. Heat Mass Transfer, **131**, pp. 558–573.

[5] Gescheit, I. M., Dayan, A., Ben-David, M., and Gannot, I., 2009, "Minimal-Invasive Thermal Imaging of a Malignant Tumor: A Simple Model and Algorithm," Med. Phys., **37**(1), pp. 211–216.

[6] Han, F., Shi, G., Liang, C., Wang, L., and Li, K., 2015, "A Simple and Efficient Method for Breast Cancer Diagnosis Based on Infrared Thermal Imaging," Cell Biochem. Biophys., **71**(1), pp. 491–498.

[7] Ye, F., and Shi, G. L., 2012, "Clinical Breast Cancer Analysis With Surface Fitting in the Medical Thermal Texture Maps," Appl. Mech. Mater., **263–266**, pp. 2454–2457.

[8] Rastgar-Jazi, M., and Mohammadi, F., 2017, "Parameters Sensitivity Assessment and Heat Source Localization Using Infrared Imaging Techniques," BioMed. Eng. OnLine, **16**(1), p. 113.

[9] Akpolile, A., Mokobia, E., and Ikubor, J., 2021, "Analytical Approach to the Penne's Bioheat Equation for the Evaluation of Temperature for Deep Seated Tissues," Adv. Math. Sci. J., **10**(7), pp. 2957–2976.

[10] Mitra, S., and Balaji, C., 2010, "A Neural Network Based Estimation of Tumour Parameters From a Breast Thermogram," Int. J. Heat Mass Transfer, **53**(21–22), pp. 4714–4727.

[11] Saniei, E., Setayeshi, S., Akbari, M. E., and Navid, M., 2016, "Parameter Estimation of Breast Tumour Using Dynamic Neural Network From Thermal Pattern," J. Adv. Res., **7**(6), pp. 1045–1055.

[12] Hossain, S., and Mohammadi, F. A., 2016, "Tumor Parameter Estimation Considering the Body Geometry by Thermography," Comput. Biol. Med., **76**, pp. 80–93.

[13] Paruch, M., and Majchrzak, E., 2007, "Identification of Tumor Region Parameters Using Evolutionary Algorithm and Multiple Reciprocity Boundary Element Method," Eng. Appl. Artif. Intell., **20**(5), pp. 647–655.

[14] Das, K., and Mishra, S. C., 2013, "Estimation of Tumor Characteristics in a Breast Tissue With Known Skin Surface Temperature," J. Therm. Biol., **38**(6), pp. 311–317.

[15] Hatwar, R., and Herman, C., 2017, "Inverse Method for Quantitative Characterisation of Breast Tumours From Surface Temperature Data," Int. J. Hyperthermia, **33**(7), pp. 1–757.

[16] Figueiredo, A. A. A., do Nascimento, J. G., Malheiros, F. C., da Silva Ignacio, L. H., Fernandes, H. C., and Guimaraes, G., 2019, "Breast Tumor Localization Using Skin Surface Temperatures From a 2D Anatomic Model Without Knowledge of the Thermophysical Properties," Comput. Methods Programs Biomed., **172**, pp. 65–77.

[17] Bezerra, L. A., Oliveira, M. M., Rolim, T. L., Conci, A., Santos, F. G. S., Lyra, P. R. M., and Lima, R. C. F., 2013, "Estimation of Breast Tumor Thermal Properties Using Infrared Images," Signal Process., **93**(10), pp. 2851–2863.

[18] Agnelli, J. P., Barrea, A. A., and Turner, C. V., 2011, "Tumor Location and Parameter Estimation by Thermography," Math. Comput. Modell., **53**(7–8), pp. 1527–1534.

[19] Gonzalez-Hernandez, J.-L., Recinella, A. N., Kandlikar, S. G., Dabydeen, D., Medeiros, L., and Phatak, P., 2020, "An Inverse Heat Transfer Approach for Patient-Specific Breast Cancer Detection and Tumor Localization Using Surface Thermal Images in the Prone Position," Infrared Phys. Technol., **105**, p. 103202.

[20] Jiang, L., Zhan, W., and Loew, M. H., 2011, "Modeling Static and Dynamic Thermography of the Human Breast Under Elastic Deformation," Phys. Med. Biol., **56**(1), pp. 187–202.

[21] Gonzalez-Hernandez, J.-L., Kandlikar, S. G., Dabydeen, D., Medeiros, L., and Phatak, P., 2018, "Generation and Thermal Simulation of a Digital Model of the Female Breast in Prone Position," J. Eng. Sci. Med. Diagn. Ther., **1**(4), p. 041006.

[22] González, F. J., 2021, "Thermal Simulations of Cancerous Breast Tumors and Cysts on a Realistic Female Torso," J. Biomech. Eng., **143**(6), p. 061001.

[23] Montienthong, P., and Rattanadecho, P., 2019, "Focused Ultrasound Ablation for the Treatment of Patients With Localized Deformed Breast Cancer: Computer Simulation," ASME J. Heat Transfer-Trans. ASME, **141**(10), p. 101101.

[24] Zhang, X., Zheng, L., Liu, L., and Zhang, X., 2020, "Modeling and Simulation on Heat Transfer in Blood Vessels Subject to a Transient Laser Irradiation," ASME J. Heat Transfer-Trans. ASME, **142**(3), p. 031201.

[25] Zhu He, Z., Xue, X., and Liu, J., 2013, "An Effective Finite Difference Method for Simulation of Bioheat Transfer in Irregular Tissues," ASME J. Heat Transfer-Trans. ASME, **135**(7), p. 071003.

[26] Partridge, P. W., and Wrobel, L. C., 2007, "An Inverse Geometry Problem for the Localisation of Skin Tumours by Thermal Analysis," Eng. Anal. Boundary Elem., **31**(10), pp. 803–811.

[27] Manuel Luna, J., Romero-Mendez, R., Hernandez-Guerrero, A., and Elizalde-Blancas, F., 2012, "Procedure to Estimate Thermophysical and Geometrical Parameters of Embedded Cancerous Lesions Using Thermography," J. Biomech. Eng., **134**(3), p. 031008.

[28] Agnelli, J. P., Padra, C., and Turner, C. V., 2011, "Shape Optimization for Tumor Location," Comput. Math. Appl., **62**(11), pp. 4068–4081.

[29] Chebbah, N. K., Ouslim, M., and Benabid, S., 2022, "New Computer Aided Diagnostic System Using Deep Neural Network and SVM to Detect Breast Cancer in Thermography," Quant. InfraRed Thermogr. J., pp. 1–16.

[30] Mambou, S. J., Maresova, P., Krejcar, O., Selamat, A., and Kuca, K., 2018, "Breast Cancer Detection Using Infrared Thermal Imaging and a Deep Learning Model," Sensors (Basel), **18**(9), p. 2799.

[31] Ng, E. Y. K., and Kee, E. C., 2008, "Advanced Integrated Technique in Breast Cancer Thermography," J. Med. Eng. Technol., **32**(2), pp. 103–114.

[32] Raissi, M., Perdikaris, P., and Karniadakis, G. E., 2017, "Machine Learning of Linear Differential Equations Using Gaussian Processes," J. Comput. Phys., **348**, pp. 683–693.

[33] Raissi, M., Perdikaris, P., and Karniadakis, G. E., 2017, "Inferring Solutions of Differential Equations Using Noisy Multi-Fidelity Data," J. Comput. Phys., **335**, pp. 736–746.

[34] Raissi, M., Perdikaris, P., and Karniadakis, G. E., 2019, "Physics-Informed Neural Networks: A Deep Learning Framework for Solving Forward and Inverse Problems Involving Nonlinear Partial Differential Equations," J. Comput. Phys., **378**, pp. 686–707.

[35] Cai, S., Wang, Z., Wang, S., Perdikaris, P., and Karniadakis, G. E., 2021, "Physics-Informed Neural Networks for Heat Transfer Problems," ASME J. Heat Transfer-Trans. ASME, **143**(6), p. 060801.

[36] Hughes, M. T., Kini, G., and Garimella, S., 2021, "Status, Challenges, and Potential for Machine Learning in Understanding and Applying Heat Transfer Phenomena," ASME J. Heat Transfer-Trans. ASME, **143**(12), p. 120802.

[37] Pashaei Kalajahi, A., Perez-Raya, I., and D'Souza, R. M., 2022, "Physics Informed Deep Neural Net Inverse Modeling for Estimating Model Parameters in Permeable Porous Media Flows," J. Fluids Eng., **144**(6), p. 061102.

[38] Chen, H., Wang, K., Liu, Z., and Zhou, H., 2022, "Surface Temperature Analysis and Thermophysical Property Estimation for Breast Cancer by Deep Learning," Numer. Heat Transfer, Part A: Appl., **1**(1), pp. 1–17.

[39] Recinella, A. N., Gonzalez-Hernandez, J.-L., Kandlikar, S. G., Dabydeen, D., Medeiros, L., and Phatak, P., 2019, "Clinical Infrared Imaging in the Prone Position for Breast Cancer Screening—Initial Screening and Digital Model Validation," ASME J. Med. Diagn., **3**(1), p. 011005.

[40] Mukhmetov, O., Igali, D., Mashekova, A., Zhao, Y., Ng, E. Y. K., Fok, S. C., and Teh, S. L., 2021, "Thermal Modeling for Breast Tumor Detection Using Thermography," Computer Methods and Programs in Biomedicine, **183**, p. 105074.

[41] Singh, D., and Singh, A. K., 2020, "Role of Image Thermography in Early Breast Cancer Detection-Past, Present and Future," **137**, p. 109542.

[42] Fernández-Ovies, F. J., Santiago Alférez-Baquero, E., de Andrés-Galiana, E. J., Cernea, A., Fernández-Muñiz, Z., and Fernández-Martínez, J. L., 2019, "Detection of Breast Cancer Using Infrared Thermography and Deep Neural Networks," *Bioinformatics and Biomedical Engineering*, I. Rojas, O. Valenzuela, F. Rojas, and F. Ortuño, eds., Springer International Publishing, Cham, pp. 514–523.

[43] Zuluaga-Gomez, J., Al Masry, Z., Benaggoune, K., Meraghni, S., and Zerhouni, N., 2021, "A CNN-Based Methodology for Breast Cancer Diagnosis Using Thermal Images," Comput. Methods Biomech. Biomed. Eng. Imag. Vis., **9**(2), pp. 131–145.

[44] Chaves, E., Gonçalves, C. B., Albertini, M. K., Lee, S., Jeon, G., and Fernandes, H. C., 2020, "Evaluation of Transfer Learning of Pre-Trained CNNs Applied to Breast Cancer Detection on Infrared Images," Appl. Opt., **59**(17), pp. E23–E28.

[45] Sánchez-Cauce, R., Pérez-Martín, J., and Luque, M., 2021, "Multi-Input Convolutional Neural Network for Breast Cancer Detection Using Thermal Images and Clinical Data," Comput. Methods Programs Biomed., **204**, p. 106045.

[46] Husaini, M. A. S. A., Habaebi, M. H., Hameed, S. A., Islam, M. R., and Gunawan, T. S., 2020, "A Systematic Review of Breast Cancer Detection Using Thermography and Neural Networks," IEEE Access, **8**, pp. 208922–208937.

[47] Zadeh, H. G., Fayazi, A., Binazir, B., and Yargholi, M., 2020, "Breast Cancer Diagnosis Based on Feature Extraction Using Dynamic Models of Thermal Imaging and Deep Autoencoder Neural Networks," JTE, **49**(3), pp. 1516–1532.

[48] Torres-Galván, J. C., Guevara, E., Kolosovas-Machuca, E. S., Oceguera-Villanueva, A., Flores, J. L., and González, F. J., 2022, "Deep Convolutional Neural Networks for Classifying Breast Cancer Using Infrared Thermography," Quant. InfraRed Thermogr. J., **19**(4), pp. 283–294.

[49] Gautam, N., Singh, A., Kumar, K., and Aggarwal, P. K., 2021, "Investigation on Performance Analysis of Support Vector Machine for Classification of Abnormal Regions in Medical Image," J. Ambient Intell. Human Comput., **1**(1), pp. 1–10.

[50] Gautherie, M., 1980, "Thermopathology of Breast Cancer: Measurement and Analysis of In Vivo Temperature and Blood Flow," Ann. New York Acad. Sci., **335**(1), pp. 383–415.

[51] Lozano, A., Hayes, J. C., Compton, L. M., Azarnoosh, J., and Hassanipour, F., 2020, "Determining the Thermal Characteristics of Breast Cancer Based on High-Resolution Infrared Imaging, 3D Breast Scans, and Magnetic Resonance Imaging," Sci. Rep., **10**(1), p. 10105.
[52] Duck, F. A., 2013, *Physical Properties of Tissues: A Comprehensive Reference Book*, Academic Press, New York.
[53] Fathi, M. F., Perez-Raya, I., Baghaie, A., Berg, P., Janiga, G., Arzani, A., and D'Souza, R. M., 2020, "Super-Resolution and Denoising of 4D-Flow MRI Using Physics-Informed Deep Neural Nets," Comput. Methods Programs Biomed., **197**, p. 105729.
[54] Rao, C., Sun, H., and Liu, Y., 2020, "Physics-Informed Deep Learning for Incompressible Laminar Flows," Theor. Appl. Mech. Lett., **10**(3), pp. 207–212.
[55] Gershenson, M., and Gershenson, J., 2022, "Use of Components Analysis to Identify Internal Heat in Breast Dynamic Thermal Images," SPIE Proceedings Volume 12109, Thermosense: Thermal Infrared Applications XLIV, FL, p. 121090K.